

## Tunnel current noise spectra of spins in individual dimers of molecular radicals

Yishay Manassen <sup>1,2</sup>, Moamen Jbara <sup>1,3</sup>, Michael Averbukh,<sup>1</sup> Zion Hazan <sup>1</sup>, Carsten Henkel <sup>4</sup>, and Baruch Horovitz <sup>1,2</sup>

<sup>1</sup>*Department of Physics, Ben Gurion University of the Negev, Beer Sheva 84105, Israel*

<sup>2</sup>*The Ilse Katz Institute for Nanoscale Science and Technology, Ben-Gurion University of the Negev, Beer Sheva 84105, Israel*

<sup>3</sup>*Department of Chemistry, Technion, Haifa 32000, Israel*

<sup>4</sup>*University of Potsdam, Institute of Physics and Astronomy, 14476 Potsdam, Germany*



(Received 24 January 2022; revised 3 May 2022; accepted 6 June 2022; published 28 June 2022)

We report the detection of electron spin resonance (ESR) in individual dimers of the stable free radical 2,2,6,6-tetramethyl-piperidine-1-oxyl (TEMPO). ESR is measured by the current fluctuations in a scanning tunneling microscope (ESR-STM method). The multipeak power spectra, distinct from macroscopic data, are assigned to dimers having exchange and Dzyaloshinskii-Moriya interactions in the presence of spin-orbit coupling. These interactions are generated in our model by interfering electronic tunneling pathways from tip to sample via the dimer's two molecules. This is the first demonstration that tunneling via two spins is a valid mechanism of the ESR-STM method.

DOI: [10.1103/PhysRevB.105.235438](https://doi.org/10.1103/PhysRevB.105.235438)

### I. INTRODUCTION

The attempt to detect and manipulate a single spin in individual molecules is a fundamental challenge [1–5]. A promising tool to monitor the electron spin resonance (ESR) on the nanometer scale is based on a scanning tunneling microscope (STM) that measures current-current correlations in a static magnetic field (ESR-STM) [6–12], rather than using external radio frequency (rf) fields. The experiments so far resulted in a signal at the Larmor frequency, a signal that is sharp even at room temperature and whose frequency varies linearly with the applied magnetic field [9,11]. Such a current spectrum has been observed in several spin systems, including dangling bonds [6,7], metal impurities in silicon [8], and adsorbed paramagnetic molecular radicals [9,10]. On the Si(111)7 × 7 surface, two peaks show up and relate to defects that differ in STM images [11,12]. ESR-STM has been used to detect the hyperfine spectrum of a single spin in SiC [13,14]. Similarity to macroscopic ESR was demonstrated in the spectrum of silicon vacancy [14], showing hyperfine contributions from <sup>29</sup>Si nuclei.

Recently, a different type of ESR-STM was observed at low temperatures, using a spin-polarized tip and rf irradiation [15–18]. Furthermore, single spin ENDOR (electron nuclear double resonance) was performed [19] by applying an rf field at frequencies of the nuclear transitions and monitoring the intensity of the hyperfine line observed by ESR-STM; this facilitated measurements of the hyperfine coupling, the quadrupole coupling, and the nuclear *g* factors.

Several theoretical models for ESR-STM have been put forward [20–24], and it was shown that tunneling via a single spin cannot explain the observations [20,21]. Instead there must be at least two tunneling channels in parallel (see Fig. 1) that interfere and generate ESR-STM [20,21,24]. The two channels are most likely due to two distinct spin sites: One is the target scanned by the STM probe, while the other is possibly located on the tip itself. The lack of direct evidence

for the second spin has made elusive the interpretation of the experiments.

In the present work we consider a system of 2,2,6,6-tetramethyl-piperidine-1-oxyl (TEMPO) molecules that tend to agglomerate and are likely to form dimers (see Fig. 2). The TEMPO molecule is a stable free radical carrying a spin 1/2, hence a dimer would be an ideal setup for forming parallel tunneling routes that lead to the ESR-STM phenomenon. In our experiment, neither tip nor substrate are spin polarized and rf radiation is not applied. We find spectra of the tunneling current where the Larmor resonance is split into more than six peaks. These can be assigned to two spins, i.e., a dimer, subject to hyperfine splitting and effective interactions induced by the tunneling process into the electrodes. We model the data with a master equation developed for the electronic environment [24,25] (see Fig. 1). Our theory provides a general framework for describing the ESR-STM phenomenon for any pair of spins, be it radical molecules, impurity atoms, or quantum dots, in particular it accounts for our experimental data on TEMPO with reasonable parameters. We note also that the dimer scenario is of much interest to quantum information science, since by tuning parameters, a long-lived dark state is available and quantum entanglement can be achieved [25].

### II. EXPERIMENT

The STM is a homemade conventional Demuth-type STM as described elsewhere [19]. An impedance matching circuit is essential for transferring the rf signal from 10<sup>8</sup> Ω at the STM to 50 Ω at readout. To compensate for the huge reduction in voltage, an active circuit creates a larger voltage at readout which is uniform over the required range of frequencies (broadband impedance matching).

The experiment includes a field modulation of amplitude 0.05 G and frequency  $\omega_m/2\pi = 30$  kHz. Any field-dependent resonance is frequency modulated so that the ESR spectrum,

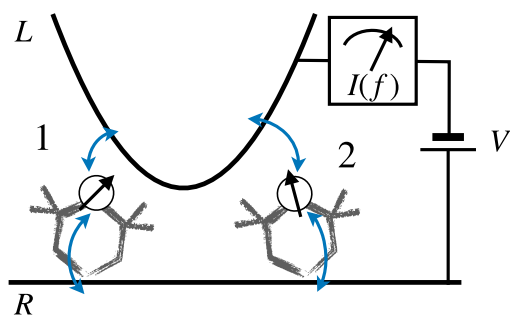


FIG. 1. Two TEMPO molecules with unpaired electrons are loosely adsorbed on a Au substrate [see Fig. 2(d) for the chemical structure]. A tip is scanned and held at a relative voltage  $V$ , providing an electronic environment for the two localized spins. The tunneling current  $I$  passes in parallel via the molecules causing spin flips, and its fluctuations reveal the level structure of the spins.

as measured by the spectrum analyzer, has a component  $S'(\omega) \cos \omega_m t$ . A lock-in amplifier identifies the spectral derivative  $S'(\omega)$  which is integrated to produce our data. This modulation method ensures that only field-dependent spectral features are detected. In the ESR-STM experiments we performed, the molecules are deposited on gold films of thickness 100 nm on Mica [26]. TEMPO is dissolved in toluene and drop casted on the surface at a concentration of 0.041 g/25 ml, corresponding to one monolayer. After drop casting the sample is put in a UHV chamber (pressure range  $10^{-10}$  torr), and

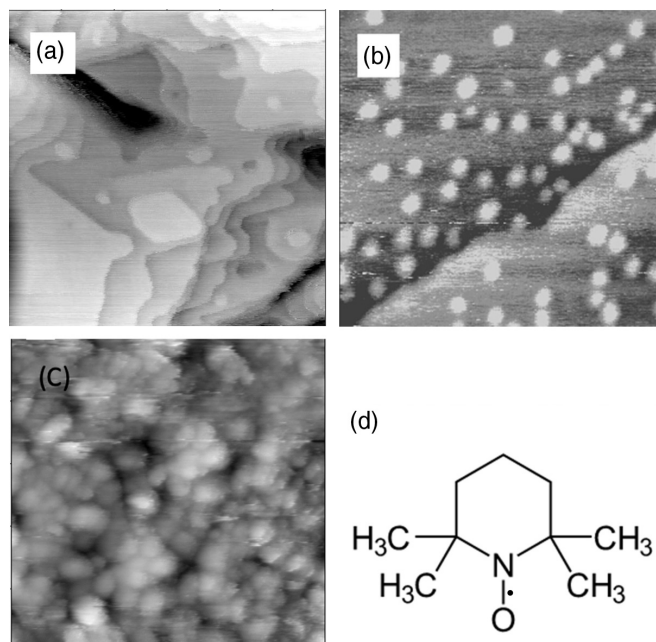


FIG. 2. (a) STM image of the Au(111) surface before deposition of TEMPO. (b) Au(111) after deposition with single molecules. (c) TEMPO adsorbed on Au(111) after spectral data acquisition. Images (a) and (b) are  $30 \times 30 \text{ nm}^2$  while image (c) is  $10 \times 10 \text{ nm}^2$ . Tunneling conditions: (a)  $-1 \text{ V}$ ,  $0.4 \text{ nA}$ ; (b)  $-0.1 \text{ V}$ ,  $0.5 \text{ nA}$ ; (c)  $-0.5 \text{ V}$ ,  $0.5 \text{ nA}$ . (d) The molecular structure of TEMPO. The unpaired electron occupies a  $p_z$  orbital on the N – O bond [29].

tunneling probe data are taken at room temperature. The clean Au surface shows flat terraces of variable shape, some of them triangular [Fig. 2(a)]. After deposition, the molecules disperse as individual entities fairly uniformly on the surface [Fig. 2(b)] and tend to agglomerate within a few hours, yet individual molecules are still seen [Fig. 2(c)]. Our spectra are taken shortly before the configuration of Fig. 2(c). STM studies of TEMPO adsorbed on Si(111) $7 \times 7$  have shown that the molecule adsorbs with its NO axis [Fig. 2(d)] normal to the surface [27]. More relevant here are studies of TEMPO with Au spheres, showing the disappearance of the ESR signal when the NO group is close to the Au surface [28]. The probability that two NO groups are near each other is small so that the formation of directly interacting spins, e.g., via dipole-dipole interactions, can be neglected. In our setup, we only need that the half-filled NO orbitals are close to the tip and to the substrate to allow for parallel tunneling: The interactions are then generated via these tunneling processes.

The  $g$  tensor and hyperfine coupling of TEMPO are well documented [29], showing an almost isotropic  $g$  factor  $g \approx 2.007$  (within .5%). The eigenvalues of the hyperfine interaction with the nuclear  $^{14}\text{N}$  spin are 17, 15, and 94 MHz for the  $x$ ,  $y$ , and  $z$  directions, respectively (the singly occupied p orbital of N defines the  $z$  axis). The dominant hyperfine coupling  $a$  in the direction parallel to the magnetic field depends on the molecular orientation and possibly on averaging due to rotational motion. Hence  $a$  is a fitted parameter that turns out to be 50–80 MHz between various molecular sites. The nominal external magnetic field, perpendicular to the surface, is 230 G, which with  $g = 2$  would correspond to a Larmor frequency of  $\nu = 644 \text{ MHz}$ , yet we take  $\nu$  as a fitting parameter, allowing for uncertainties in the actual field. Experimental spectra of the tunnel current are taken in 9800 channels (points in the spectrum analyzer) covering the range of 580–780 MHz, each channel requiring about  $50 \mu\text{s}$  acquisition time. This is short compared to the spin lifetime of the  $^{14}\text{N}$  nucleus, typically in the range of 0.5–1 ms (Ref. [30]), so that we may assume fixed spin states. The spectrum analyzer averages 200 spectra, however, so that eventually nuclear spin flips occur, and an ensemble of all levels is probed. A whole spectrum of a single site takes 90 s.

The data for a clean Au surface (Fig. 3) shows no magnetic field-dependent modes in our frequency range; in this case field modulation is not applied since both a 230-G field as well as zero field are measured. Data including deposited TEMPO molecules (using modulation) is exhibited below, together with theory fits.

The ESR of two TEMPO molecules depends sensitively on the hyperfine interaction. The molecule has three  $^{14}\text{N}$  nuclear spin states whose hyperfine coupling to the unpaired electron spin splits the ESR into  $\nu$ ,  $\nu \pm a$ . A dimer with two spins has then nine hyperfine states with nuclear spin projections  $m$ ,  $m' = 0, \pm 1$ . When electrons transit between the electrodes (tip and substrate) through two TEMPO molecules, exchange tunneling events occur and generate interactions between the two molecular spins as well as dissipation (linewidth  $\Gamma$ ) [24,25]. Both interactions and dissipation depend sensitively on the energy levels of the two molecules being either degenerate ( $m = m'$ ) or nondegenerate ( $m \neq m'$ ). We assume that  $a \gg \Gamma$  (confirmed by our analysis) so that the

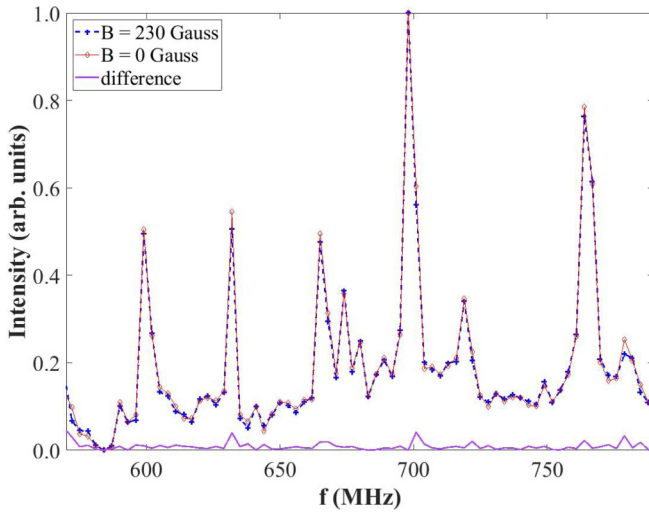


FIG. 3. ESR-STM data on a clean Au surface with a field of 230G and without a field. The absolute value of the difference is also shown.

distinction between the two types is well defined. In the three degenerate states, more (secular) terms contribute to the master equation and generate a stronger exchange interaction (as compared with nondegenerate states), as well as Dzyaloshinskii-Moriya interactions [25]. The ESR-STM spectra we take result from an ensemble average over both cases, leading in general to overall eight peaks for a given dimer. We note that the behavior in the relatively prominent dips between the peaks is most informative: Their positions determine the bare hyperfine parameter, and their shapes are sensitive to couplings among degenerate pairs.

### III. MODEL

We review first a generic model, that has two spin sites, each tunnel coupled to the tip as well as to the substrate (Figs. 1 and 4). The spins have Larmor frequencies  $\nu_1, \nu_2$  that

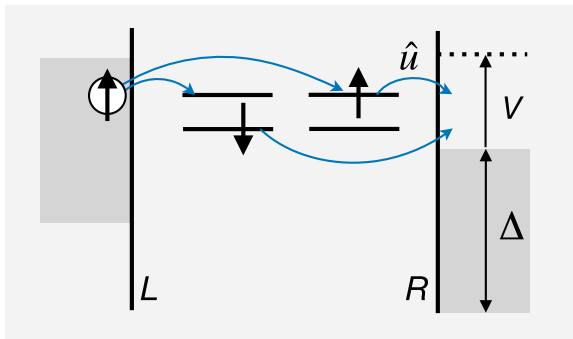


FIG. 4. Illustration of an exchange-tunneling process between  $L, R$  electrodes (tip and substrate) via two localized spins in parallel. An electron tunneling from the  $L$  electrode is spin flipped at one localized spin site while it is not spin flipped at the other localized spin site. In addition the latter spin is rotated by the spin-orbit interaction upon tunneling into the  $R$  electrode, represented by the unitary  $\hat{u}$ .

may or may not be equal. The Hamiltonian has the form,

$$\begin{aligned}\mathcal{H} &= \mathcal{H}_0 + \mathcal{H}_L + \mathcal{H}_R + \mathcal{H}_{xt}, \\ \mathcal{H}_0 &= \frac{1}{2}\nu_1\tau_z \otimes \mathbb{1} + \frac{1}{2}\nu_2\mathbb{1} \otimes \tau_z, \\ \mathcal{H}_{xt} &= J_1c_R^\dagger\sigma c_L \cdot \tau \otimes \mathbb{1} + J_2c_R^\dagger\hat{\sigma}c_L \cdot \mathbb{1} \otimes \tau + \text{H.c.},\end{aligned}\quad (1)$$

where  $\nu_{1,2}$  involve the nuclear quantum numbers  $m, m'$ , as spelled out in Eqs. (3) and (4) below.  $\mathcal{H}_L, \mathcal{H}_R$  correspond to noninteracting electrons on the tip ( $L$ ) and substrate ( $R$ ), respectively. The exchange-tunneling Hamiltonian  $\mathcal{H}_{xt}$ , sketched in Fig. 4, involves local operators  $c_L, c_R$  for the tunneling electrons on the tip and substrate, respectively,  $\sigma, \tau$  are Pauli matrices for the tunneling electrons and either of the two localized spins, the tensor product of the latter corresponds to spin 1  $\otimes$  spin 2. The hopping terms  $J_{1,2}$  in Eq. 1 are derived from tunneling via a localized state that has strong on-site Coulomb repulsion, which eliminates doubly occupied or zero occupied electron states, a procedure known as the Schrieffer-Wolff transformation [24,31]. For spin 2, the hopping involves angles  $\theta, \phi$  of a unitary matrix  $\hat{u} = e^{i\sigma_z\phi}e^{i\sigma_y\theta/2}$  that represents spin-orbit interactions. The spin-orbit interaction is essential for allowing the current-spin coupling [24] and also affects the effective interactions [25] [see Eq. (2)].

The system-bath model defined by the Hamiltonian  $\mathcal{H}$  has been treated in Refs. [24,25] within a Born-Markov master equation. The tunneling elements generate linewidths  $\Gamma_1, \Gamma_2$  for either spin, and remarkably, also effective spin-spin interactions. They contain an exchange coupling  $J_{\text{ex}}$  and a Dzyaloshinskii-Moriya coupling  $J_{\text{DM}}$  given by

$$\left. \begin{matrix} J_{\text{ex}} \\ J_{\text{DM}} \end{matrix} \right\} = 4J_1J_2N^2(0)\Delta \cos\frac{1}{2}\theta \begin{cases} \cos\phi \\ \sin\phi \end{cases}, \quad (2)$$

and are spelled out in Eqs. (3) and (4). These couplings can be fairly large as they depend on the electron bandwidths in the electrodes  $\Delta$  (Fig. 4);  $N(0)$  is the density of states of either electrode. The resulting master equations for the density matrix are presented in the Appendix.

The effective interactions depend on  $\nu_1, \nu_2$  being degenerate or not. This is determined by the hyperfine couplings. We keep in  $\mathcal{H}_0$  the hyperfine component  $a$  that is parallel to the magnetic field, a transverse hyperfine coupling  $b$  can be neglected since it affects the spectra only in second order  $\sim(b/\nu_{1,2})^2$ . Such terms may cause a small difference between the two hyperfine splittings and even shift  $\nu_{1,2}$ . The eigenenergies that appear in  $\mathcal{H}_0$  are  $\nu_1 = \nu + am$  and  $\nu_2 = \nu + am'$  where the fixed quantum numbers  $m, m' = 0, \pm 1$  label the nuclear spin states. In the degenerate case  $m = m'$ , the effective Hamiltonian (apart of dissipative terms) is

$$\begin{aligned}\mathcal{H}_{\text{deg}} &= \frac{1}{2}(\nu + am)[\tau_z \otimes \mathbb{1} + \mathbb{1} \otimes \tau_z] \\ &\quad - J_{\text{ex}}\tau \otimes \tau + J_{\text{DM}}[\tau_x \otimes \tau_y - \tau_y \otimes \tau_x],\end{aligned}\quad (3)$$

with the exchange and DM couplings defined in Eq. (2). The eigenstates, levels, and transition frequencies are listed in Table I. Note that the hyperfine transitions  $\nu + am, m = 0, \pm 1$  are split by the interactions. In particular  $J_{\text{DM}}$  is responsible for the splitting of the  $T1 \rightarrow T2, T2 \rightarrow T3$  transitions.

The nondegenerate dimer states  $m \neq m'$  have an anisotropic exchange coupling (being the only secular

TABLE I. Spectra and transitions of degenerate dimers (first four lines where  $\tan \psi = J_{\text{DM}}/J_{\text{ex}}$ ,  $J = \sqrt{J_{\text{ex}}^2 + J_{\text{DM}}^2}$ , and nuclear levels  $m = m' = -1, 0, 1$ ) and nondegenerate dimers (last line where  $s, s' = \pm 1$  are electron spin states). The  $S, T$  notation refers to singlet or triplet states that decouple exactly in the limit  $J_{\text{DM}} = 0$ . Transitions are given only near the Larmor frequency  $\nu$ .

Eigenstates	Energy levels	Transition frequencies
$S :  \uparrow\downarrow mm\rangle - e^{i\psi}  \downarrow\uparrow mm\rangle$	$2J + J_{\text{ex}}$	$S \rightarrow T1, T3 :$
$T1 :  \uparrow\uparrow mm\rangle$	$\nu - J_{\text{ex}} + am$	$(\nu + am) \pm 2(J + J_{\text{ex}})$
$T2 :  \uparrow\downarrow mm\rangle + e^{i\psi}  \downarrow\uparrow mm\rangle$	$-2J + J_{\text{ex}}$	$T1 \rightarrow T2, T2 \rightarrow T3 :$
$T3 :  \downarrow\downarrow mm\rangle$	$-v - J_{\text{ex}} - am$	$\nu + am \pm 2(J - J_{\text{ex}})$
$ ss'm \neq m'\rangle$	$\frac{1}{2}s(\nu + am) + \frac{1}{2}s'(\nu + am') - ss'J_{\text{ex}}$	$\nu + am \pm 2J_{\text{ex}}$

term [25]), and the effective Hamiltonian is

$$\mathcal{H}_{\text{nondeg}} = \frac{1}{2}(\nu + am)\tau_z \otimes \mathbb{1} + \frac{1}{2}(\nu + am')\mathbb{1} \otimes \tau_z - J_{\text{ex}}\tau_z \otimes \tau_z. \quad (4)$$

The spectrum and transition frequencies are listed in Table I. Also in this case the hyperfine transitions are split by the interactions.

The fluctuations in the tunneling current arise from spin flips. We model these by time correlations of two spin operators, one carries a current with spin flip  $\tau_{\pm}$ , the other carrying a current without spin flip  $\tau_z$ . (There are additional combinations from flips of both spins [25], but outside our frequency range and not considered here.) Hence the current correlations are proportional to

$$C_2(\nu_1, \nu_2, \omega) = \langle (\tau_- \otimes \tau_z)_t (\tau_+ \otimes \tau_z)_0 \rangle_{\omega} + \langle (\tau_z \otimes \tau_-)_t (\tau_z \otimes \tau_+)_0 \rangle_{\omega} + (+ \leftrightarrow -), \quad (5)$$

where  $\langle \dots \rangle_{\omega}$  is a Fourier transform. The frequency parameters  $\nu_{1,2}$  in Eq. (5) depend on  $m, m'$  of the two nuclear spins, i.e., they are either of  $\nu, \nu \pm a$ . Note that interchanging  $\nu_1, \nu_2$  yields distinct results, e.g., if  $\Gamma_1 \neq \Gamma_2$ . For all nuclear configurations of a dimer, the nondegenerate (six pairs) and degenerate (three pairs) contributions are

$$C_{\text{nondeg}}(\omega) = \sum_{\pm} [C_2(\nu \pm a, \nu, \omega) + C_2(\nu \pm a, \nu \mp a, \omega) + C_2(\nu, \nu \pm a, \omega)],$$

$$C_{\text{deg}}(\omega) = \sum_{m=0, \pm 1} C_2(\nu + ma, \nu + ma, \omega). \quad (6)$$

The total observable is  $C_{\text{nondeg}}(\omega) + C_{\text{deg}}(\omega)$ .

We evaluate the spin-spin correlations via the master equation for both the degenerate and nondegenerate cases, as

summarized in the Appendix, and fit parameters to the experimental data. We consider first the general features of the theoretical results, an example is in Fig. 5(left). The dominant terms are the six nondegenerate terms (higher red lines) that are split by  $\pm 2J_{\text{ex}}$ . Between these six peaks are strong dips at the bare (noninteracting) hyperfine transitions  $\nu, \nu \pm a$ , thus readily determining these parameters. The degenerate terms (lower black lines) split from the bare transitions by both a strong and a weak splitting  $\pm 2(J \pm J_{\text{ex}})$  (see Table I). The weak splitting  $2(J - J_{\text{ex}}) > 0$  arises from  $J_{\text{DM}}$ ; if the latter vanishes, some lines do not split and there would be a (small) peak in the bare locations. Since this was not seen in any of our data we conclude that  $J_{\text{DM}}$  is significant, i.e., at least of order  $J_{\text{ex}}$ . The weak splittings produce side shoulders on the main peaks, seen in some of our data. The strong splitting is larger than that of the nondegenerate terms ( $2(J + J_{\text{ex}}) > 2J_{\text{ex}}$ ), hence, although the overall intensity of the degenerate terms is weaker, the peaks at the edges of the spectrum become distinct and dominant, leading in general to an apparent eight-peak structure.

#### IV. ANALYSIS AND DISCUSSION

Before fitting our data, we note that macroscopic ESR for dimers with exchange is totally different from that above. In the macroscopic case a homogeneous rf field is applied so that the measured correlations are symmetric in both spins,  $\langle (\tau_- \otimes \tau_z + \tau_z \otimes \tau_-)_t (\tau_+ \otimes \tau_z + \tau_z \otimes \tau_+)_0 \rangle_{\omega}$ . The permutation symmetry forbids in particular  $S \rightarrow T$  transitions for  $m = m'$  and  $J_{\text{DM}} = 0$ . Furthermore, in the STM case the exchange is generated via the electrodes and is different for degenerate and nondegenerate pairs [compare Eqs. (3) and (4)], while in the macroscopic case, there is a direct exchange that applies

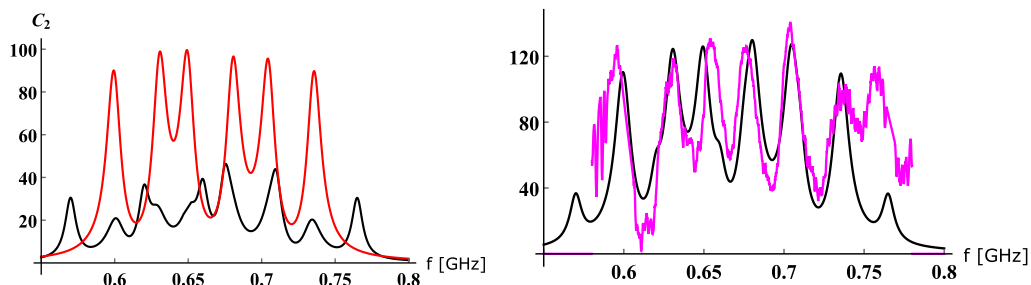


FIG. 5. (Left) Theoretical spectra of nondegenerate spin pairs (upper red line) and of degenerate ones (lower black line) vs  $f = \omega/2\pi$ . (Right) Experimental (magenta) and theory (black) spectra, the latter being the sum of the spectra on the left. Fitting parameters in MHz:  $\nu : 665, a : 50, 55, J_{\text{ex}} : 8, J_{\text{DM}} : 9$ ; hyperfine  $a$  is somewhat different between left and right.

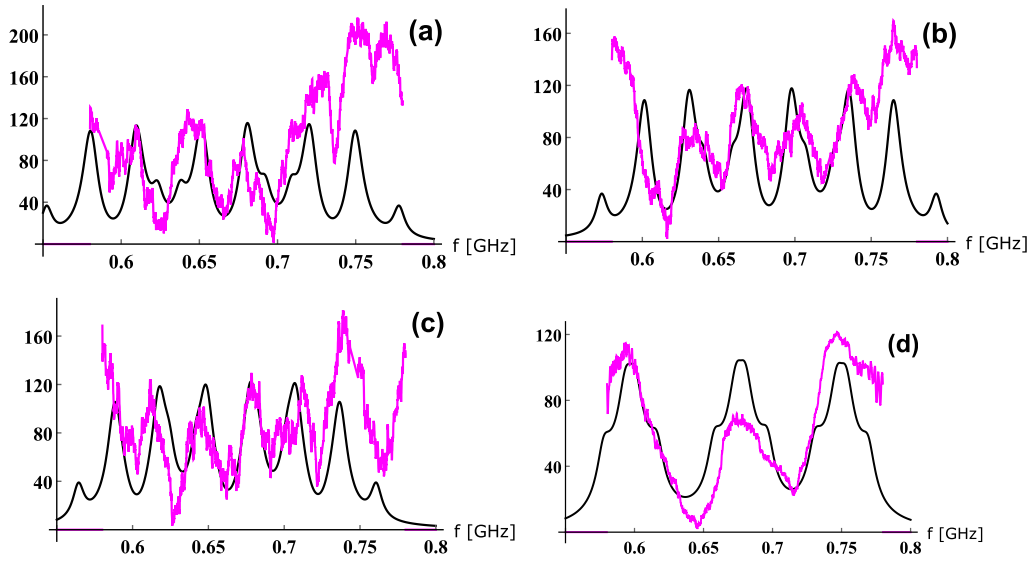


FIG. 6. Experimental ESR-STM spectra (jagged magenta lines) and fitted theoretical curves using the following parameters (in MHz): (a)  $\nu$  : 666,  $a$  : 71, 69,  $J_{\text{ex}}$  : 7,  $J_{\text{DM}}$  : 12. (b)  $\nu$  : 683,  $a$  : 67,  $J_{\text{ex}}$  : 7,  $J_{\text{DM}}$  : 12. (c)  $\nu$  : 663,  $a$  : 60, 59,  $J_{\text{ex}}$  : 7,  $J_{\text{DM}}$  : 10. (d)  $\nu$  : 677,  $a$  : 80, 73,  $J_{\text{ex}}$  : 1,  $J_{\text{DM}}$  : 8. The small differences in  $a$  correspond to different nuclear  $m$  levels and may arise from second-order shifts due to subleading hyperfine couplings. The data corresponds to total current of 0.1 nA and tip-substrate voltage of 1 V (positive substrate).

equally to all  $m$ ,  $m'$ . Finally, the spin-orbit interaction responsible for the coupling  $J_{\text{DM}}$  is most likely generated by the heavy metal atoms in the tip, hence absent in a macroscopic setup.

The experimental spectra are restricted by the detection sensitivity of the impedance matching circuits to the frequencies 580–780 MHz, and some knowledge on the ESR parameters, e.g., Larmor frequencies and hyperfine couplings is needed to choose the proper spectral window. The fit to theory is best when the spectrum covers a wide range, i.e., probing all possible eigenfrequencies. We have included in our analysis only data that have at least seven peaks [except for Fig. 6(d)]; we have found 15 such spectra. We have excluded other spectra with four to six lines, as some peaks are likely to be outside the measured range, due to stronger interactions. We note that monomer molecules require an additional spin species, possibly at a remote Larmor frequency, to generate an interference (Fig. 1 and Ref. [24]); this situation is likely to have an exchange term as in Eq. (4), leading to six lines in our spectral range. The latter case may also correspond to a dimer situation, hence we have excluded this case. We did not see spectra with only three lines; note, however, the peculiar data in Fig. 6(d), which we attribute to a dimer (see below). Figure 5 (right) shows the theory spectrum (black smooth line), the sum of the two curves in Fig. 5 (left), compared to experimental data, the magenta jagged curve. The parameters of the fit are given in the caption, in addition we use the linewidths  $\Gamma_1, \Gamma_2 \approx 4$  MHz. (Note that in the absence of splitting due to  $J_{\text{ex}}$  and  $J_{\text{DM}}$ , the linewidth becomes  $\Gamma_1 + \Gamma_2$ .) These linewidths also determine the tunneling current via both spin sites [24]  $\frac{3}{8}e(\Gamma_1 + \Gamma_2) \approx 0.5$  pA. We expect then that most of the total current (0.1 nA) tunnels directly from tip to substrate, indeed dominant as it is not Coulomb blocked.

Figures 6(a)–6(c) show additional fitting curves with fairly similar parameters, obtained for different spots on the

sample. In all cases, reasonable agreement is found with realistic fit parameters; note in particular that the couplings  $J_{\text{ex}}$ ,  $J_{\text{DM}}$  are comparable in magnitude, which points, on the basis of the model, towards a sizable rotation angle  $\tan \phi \sim 1$  in the spin-orbit interaction. The fitted values of  $a$  are in between the hyperfine eigenvalues for the  $z$  and  $x, y$  axes [29]. This suggests some tilt or rotational averaging of the molecular  $z$  axis relative to the magnetic field (normal to the surface). We have assumed that the molecules of a given dimer have the same  $a$  parameter, as justified by the fits; this implies that they are similarly tilted.

An exception is Fig. 6(d) that appears to have only three peaks, as if  $J_{\text{ex}} = J_{\text{DM}} = 0$ . Fitting the data this way would yield linewidths  $\Gamma_1, \Gamma_2$  much larger than in all other cases, however. We believe that it is more likely that a weak, but finite exchange applies in this case [caption of Fig. 6(d)], causing shoulders and an apparent increase in width of these lines.

In conclusion, we have found a large set of ESR-STM spectra that fit well to a theory of two spins located on a molecular dimer and coupled via electrons that tunnel between tip and substrate. The fitting parameters give effective exchange and Dzyaloshinskii-Moriya couplings that are of the same order and fairly strong (even comparable to the hyperfine splitting, using the conventional definitions  $4J_{\text{ex}}, 4J_{\text{DM}}$  of Ref. [32]). Our analysis of these dimers opens a route for studying hyperfine interactions and  $g$  factors in molecules and determining their parameters. It also paves the road to measure spin-orbit coupling for tunneling electrons.

## ACKNOWLEDGMENTS

This project has received funding from the ATTRACT initiative within the European Union's Horizon 2020 research and innovation programme under Grant Agreement No. 777222, project NMR1. Additional funding was provided by the Israel Science Foundation collaboration with

China, Grant No. 2811/19, and the Deutsche Forschungsgemeinschaft (DFG, Germany), Project No. 282981637. C.H. and B.H. gratefully acknowledge funding by the Deutsche Forschungsgemeinschaft through the DIP programme (Grant No. Fo 703/2-1).

### APPENDIX: MASTER EQUATIONS

We present in this Appendix the full Hamiltonian and the master equations that are used to find the spin correlations. We consider two isolated spins (quantum dots or impurities) described by Pauli matrices  $\boldsymbol{\tau} \otimes \mathbb{1}$  and  $\mathbb{1} \otimes \boldsymbol{\tau}$  (tensor products display operators acting on the first spin and those acting on the second spin) coupled by tunneling in parallel to two environments  $L$ ,  $R$  (tip and substrate for the STM setup). The latter have spin-independent energies  $\epsilon_{kL}$ ,  $\epsilon_{kR}$  whose chemical potentials differ by a bias  $V$ , and Hamiltonian  $\mathcal{H}_L = \sum_k \epsilon_{kL} c_{kL}^\dagger c_{kL}$ , with electron creation and annihilation operators  $c_{kL}^\dagger$ ,  $c_{kL}$ , being two-component spinors for each mode  $kL$ ; similarly with  $L \rightarrow R$ . The Hamiltonian has two forms, depending on the two Larmor frequencies being either degenerate  $\nu$  or nondegenerate  $\nu_1 \neq \nu_2$  such that  $|\nu_1 - \nu_2| \gg \Gamma_{1,2}$ , where  $\Gamma_{1,2}$  are linewidths (to be identified below). The isolated spin Hamiltonian is then of either form (using  $\hbar = 1$ ):

$$\begin{aligned} \mathcal{H}_0 &= \frac{1}{2} \nu (\tau_z \otimes \mathbb{1} + \mathbb{1} \otimes \tau_z) && \text{degenerate case;} \\ \mathcal{H}_0 &= \frac{1}{2} \nu_1 \tau_z \otimes \mathbb{1} + \frac{1}{2} \nu_2 \mathbb{1} \otimes \tau_z && \text{nondegenerate case.} \end{aligned} \quad (\text{A1})$$

The full Hamiltonian is

$$\begin{aligned} \mathcal{H} &= \mathcal{H}_0 + \mathcal{H}_L + \mathcal{H}_R + (J_1 c_R^\dagger \boldsymbol{\sigma} c_L \\ &\quad \cdot \boldsymbol{\tau} \otimes \mathbb{1} + J_2 c_R^\dagger \boldsymbol{\sigma} \hat{u} c_L \cdot \mathbb{1} \otimes \boldsymbol{\tau} + \text{H.c.}), \end{aligned} \quad (\text{A2})$$

where  $c_L = \sum_k c_{kL}$  is the local operator that couples to the spins (same with  $L \rightarrow R$ ). The hopping terms  $J_{1,2}$  in Eq. (A1) are derived from tunneling via a localized state that has strong

on-site Coulomb repulsion, which eliminates doubly occupied or zero occupied electron states, a procedure known as the Schrieffer-Wolff transformation [24,31]. For spin 2, we use the unitary matrix  $\hat{u} = e^{i\sigma_z \phi} e^{i\sigma_y \theta/2}$  to model spin-orbit interactions; this is important for the coupling of an STM current to the spins [24]. There are additional terms that tunnel electrons from one lead and back to the same lead, however, the terms in (A1) dominate at large voltage, i.e.,  $eV \gg \nu$ ,  $k_B T$  or  $eV \gg \nu_1, \nu_2, k_B T$  ( $T$  is temperature), the typical case in STM experiments.

The density matrix is a  $4 \times 4$  matrix and is expanded as  $\rho(t) = \sum_{\alpha, \beta} \rho_{\alpha, \beta}(t) \tau_\alpha \otimes \tau_\beta$ , with  $\alpha, \beta = 0, z, +, -$  so that  $\tau_\alpha = \mathbb{1}, \tau_z, \tau_+, \tau_-$  and  $\rho_{00} = \frac{1}{4}$ . The time evolution of the density matrix, i.e., the master equation, is derived by the Lindblad method and is detailed in Ref. [25]. It is based on integrating out the fermionic degrees of freedom of the environment, keeping only secular terms arising from the interaction (they produce transition rates between states of the two-spin system). Depending on the degeneracy, the number of secular terms differs. The tunneling terms  $J_{1,2}$  generate a spin-spin interaction  $\mathcal{H}_{\text{int}}$ , so that the master equation has in general the form,

$$\frac{d\rho}{dt} = -i[\mathcal{H}_{\text{int}}, \rho] + R\rho \quad \Rightarrow \quad \frac{d\hat{\rho}}{dt} = (\hat{H}' + \hat{R}')\hat{\rho}, \quad (\text{A3})$$

where  $R$  corresponds to both  $\mathcal{H}_0$  and the dissipative part due to tunneling. The elements  $\rho_{\alpha\beta}$  can be written as a 16-entry vector  $\hat{\rho}$ , ordered as in the left-hand side of Eq. (A4) below. The commutator with  $\mathcal{H}_{\text{int}}$  and the dissipative part  $R$  can be rewritten as a  $16 \times 16$  supermatrix  $\hat{H}' + \hat{R}'$ , and the elements of  $\hat{R}'$  can be read off from the equations given below [25].

We present first the simpler nondegenerate case where the resonant terms involve only the  $\tau_z$  tunneling terms. The method produces the spin-spin interaction  $\mathcal{H}_{\text{int}} = -J_{\text{ex}} \tau_z \otimes \tau_z$  with  $J_{\text{ex}}$  defined in Eq. (2). Using the notation  $\lambda_1 = 16\pi N^2(0)J_1^2$ ,  $\lambda_2 = 16\pi N^2(0)J_2^2$ ,  $\bar{\nu}_1 = \frac{\nu_1}{eV}$ ,  $\bar{\nu}_2 = \frac{\nu_2}{eV}$  and time in units of  $1/eV$ , the following master equation is found:

$$\begin{aligned} \frac{d\rho_{00}}{dt} &= 0, \\ \frac{d\rho_{0z}}{dt} &= -\lambda_2(\rho_{0z} + \bar{\nu}_2\rho_{00}), \\ \frac{d\rho_{0+}}{dt} &= -(\lambda_2 + i\bar{\nu}_2)\rho_{0+}, \\ \frac{d\rho_{0-}}{dt} &= -(\lambda_2 - i\bar{\nu}_2)\rho_{0-}, \\ \frac{d\rho_{z0}}{dt} &= -\lambda_1(\rho_{z0} + \bar{\nu}_1\rho_{00}), \\ \frac{d\rho_{zz}}{dt} &= -(\lambda_1 + \lambda_2)\rho_{zz} - \lambda_1\bar{\nu}_1\rho_{0z} - \lambda_2\bar{\nu}_2\rho_{z0}, \\ \frac{d\rho_{z+}}{dt} &= -(\lambda_1 + \lambda_2 + i\bar{\nu}_2)\rho_{z+} - \lambda_1\bar{\nu}_1\rho_{0+}, \\ \frac{d\rho_{z-}}{dt} &= -(\lambda_1 + \lambda_2 - i\bar{\nu}_2)\rho_{z-} - \lambda_1\bar{\nu}_1\rho_{0-}, \\ \frac{d\rho_{+0}}{dt} &= -(\lambda_1 + i\bar{\nu}_1)\rho_{+0}, \end{aligned}$$

$$\begin{aligned}
\frac{d\rho_{+z}}{dt} &= -(\lambda_1 + \lambda_2 + i\bar{\nu}_1)\rho_{+z} - \lambda_2\bar{\nu}_2\rho_{+0}, \\
\frac{d\rho_{++}}{dt} &= -[\lambda_1 + \lambda_2 + \sqrt{\lambda_1\lambda_2}\cos\frac{1}{2}\theta\cos\phi + i(\bar{\nu}_1 + \bar{\nu}_2)]\rho_{++}, \\
\frac{d\rho_{+-}}{dt} &= -[\lambda_1 + \lambda_2 - \sqrt{\lambda_1\lambda_2}\cos\frac{1}{2}\theta\cos\phi + i(\bar{\nu}_1 - \bar{\nu}_2)]\rho_{+-}, \\
\frac{d\rho_{-0}}{dt} &= -(\lambda_1 - i\bar{\nu}_1)\rho_{-0}, \\
\frac{d\rho_{-z}}{dt} &= -(\lambda_1 + \lambda_2 - i\bar{\nu}_1)\rho_{-z} - \lambda_2\bar{\nu}_2\rho_{-0}, \\
\frac{d\rho_{-+}}{dt} &= -[\lambda_1 + \lambda_2 - \sqrt{\lambda_1\lambda_2}\cos\frac{1}{2}\theta\cos\phi - i(\bar{\nu}_1 - \bar{\nu}_2)]\rho_{-+}, \\
\frac{d\rho_{--}}{dt} &= -[\lambda_1 + \lambda_2 + \sqrt{\lambda_1\lambda_2}\cos\frac{1}{2}\theta\cos\phi - i(\bar{\nu}_1 + \bar{\nu}_2)]\rho_{--}.
\end{aligned} \tag{A4}$$

Identifying the various  $\nu + am$ ,  $\nu + am'$  in Eq. (4) as  $\nu_1$ ,  $\nu_2$  determines the master equation for each pair of frequencies. The individual linewidths are identified as the decay rates of  $\rho_{+0}$ ,  $\rho_{0+}$ , i.e.,  $\Gamma_1 = \lambda_1 eV$ ,  $\Gamma_2 = \lambda_2 eV$ .

The degenerate case has more secular terms. These couple also transverse spin components and generate a spin-spin interaction  $\mathcal{H}_{\text{int}} = -J_{\text{ex}}\boldsymbol{\tau} \otimes \boldsymbol{\tau} + J_{\text{DM}}[\tau_x \otimes \tau_y - \tau_y \otimes \tau_x]$ . The  $\hat{R}'$  matrix in Eq. (A3) can be identified in the following master equation,

$$\begin{aligned}
\frac{d\rho_{00}}{dt} &= 0, \\
\frac{d\rho_{0z}}{dt} &= -\lambda_2(\rho_{0z} + \bar{\nu}\rho_{00}) - \frac{1}{4}\bar{\nu}\sqrt{\lambda_1\lambda_2}\cos\frac{1}{2}\theta(e^{i\phi}\rho_{+-} + e^{-i\phi}\rho_{-+}), \\
\frac{d\rho_{0+}}{dt} &= -(\lambda_2 + i\bar{\nu})\rho_{0+} + \frac{1}{2}\bar{\nu}\sqrt{\lambda_1\lambda_2}\cos\frac{1}{2}\theta e^{i\phi}\rho_{+z}, \\
\frac{d\rho_{0-}}{dt} &= -(\lambda_2 - i\bar{\nu})\rho_{0-} + \frac{1}{2}\bar{\nu}\sqrt{\lambda_1\lambda_2}\cos\frac{1}{2}\theta e^{-i\phi}\rho_{-z}, \\
\frac{d\rho_{z0}}{dt} &= -\lambda_1(\rho_{z0} + \bar{\nu}\rho_{00}) - \frac{1}{4}\bar{\nu}\sqrt{\lambda_1\lambda_2}\cos\frac{1}{2}\theta(e^{i\phi}\rho_{+-} + e^{-i\phi}\rho_{-+}), \\
\frac{d\rho_{zz}}{dt} &= -(\lambda_1 + \lambda_2)\rho_{zz} - \lambda_1\bar{\nu}\rho_{0z} - \lambda_2\bar{\nu}\rho_{z0} + \frac{1}{2}\sqrt{\lambda_1\lambda_2}\cos\frac{1}{2}\theta(e^{i\phi}\rho_{+-} + e^{-i\phi}\rho_{-+}), \\
\frac{d\rho_{z+}}{dt} &= -(\lambda_1 + \lambda_2 + i\bar{\nu})\rho_{z+} - \lambda_1\bar{\nu}\rho_{0+} - \sqrt{\lambda_1\lambda_2}\cos\frac{1}{2}\theta e^{i\phi}(\rho_{+z} + \frac{1}{2}\bar{\nu}\rho_{+0}), \\
\frac{d\rho_{z-}}{dt} &= -(\lambda_1 + \lambda_2 - i\bar{\nu})\rho_{z-} - \lambda_1\bar{\nu}_1\rho_{0-} - \sqrt{\lambda_1\lambda_2}\cos\frac{1}{2}\theta e^{-i\phi}(\rho_{-z} + \frac{1}{2}\bar{\nu}\rho_{-0}), \\
\frac{d\rho_{+0}}{dt} &= -(\lambda_1 + i\bar{\nu})\rho_{+0} + \frac{1}{2}\bar{\nu}\sqrt{\lambda_1\lambda_2}\cos\frac{1}{2}\theta e^{-i\phi}\rho_{z+}, \\
\frac{d\rho_{+z}}{dt} &= -(\lambda_1 + \lambda_2 + i\bar{\nu})\rho_{+z} - \lambda_2\bar{\nu}\rho_{+0} - \sqrt{\lambda_1\lambda_2}\cos\frac{1}{2}\theta e^{-i\phi}(\rho_{z+} + \frac{1}{2}\bar{\nu}\rho_{+0}), \\
\frac{d\rho_{++}}{dt} &= -[\lambda_1 + \lambda_2 + \sqrt{\lambda_1\lambda_2}\cos\frac{1}{2}\theta\cos\phi + 2i\bar{\nu}]\rho_{++}, \\
\frac{d\rho_{+-}}{dt} &= -[\lambda_1 + \lambda_2 - \sqrt{\lambda_1\lambda_2}\cos\frac{1}{2}\theta\cos\phi]\rho_{+-} + \sqrt{\lambda_1\lambda_2}\cos\frac{1}{2}\theta e^{-i\phi}(2\rho_{zz} + \bar{\nu}\rho_{0z} + \bar{\nu}\rho_{z0}), \\
\frac{d\rho_{-0}}{dt} &= -(\lambda_1 - i\bar{\nu})\rho_{-0} + \frac{1}{2}\bar{\nu}\sqrt{\lambda_1\lambda_2}\cos\frac{1}{2}\theta e^{i\phi}\rho_{z-}, \\
\frac{d\rho_{-z}}{dt} &= -(\lambda_1 + \lambda_2 - i\bar{\nu})\rho_{-z} - \lambda_2\bar{\nu}\rho_{-0} - \sqrt{\lambda_1\lambda_2}\cos\frac{1}{2}\theta e^{i\phi}(\rho_{z-} + \frac{1}{2}\bar{\nu}\rho_{-0}), \\
\frac{d\rho_{-+}}{dt} &= -[\lambda_1 + \lambda_2 - \sqrt{\lambda_1\lambda_2}\cos\frac{1}{2}\theta\cos\phi]\rho_{-+} + \sqrt{\lambda_1\lambda_2}\cos\frac{1}{2}\theta e^{i\phi}(2\rho_{zz} + \bar{\nu}\rho_{0z} + \bar{\nu}\rho_{z0}), \\
\frac{d\rho_{--}}{dt} &= -[\lambda_1 + \lambda_2 + \sqrt{\lambda_1\lambda_2}\cos\frac{1}{2}\theta\cos\phi - 2i\bar{\nu}]\rho_{--}.
\end{aligned} \tag{A5}$$

Finally, the various correlation functions in Eqs. (5) and (6) of operators  $A$ ,  $B$  are derived using the regression formula,

$$\langle A(t)B(0) \rangle_\omega = -2 \operatorname{Re} \operatorname{Tr} \left( A \frac{1}{\hat{H}' + \hat{R}' + i\omega} B \rho_\infty \right), \quad (\text{A6})$$

where  $\rho_\infty$  is the steady-state density matrix which for the nondegenerate case is

$$\rho_\infty : \quad \rho_{00} = \frac{1}{4}, \quad \rho_{0z} = -\frac{1}{4}\bar{v}_2, \quad \rho_{z0} = -\frac{1}{4}\bar{v}_1, \quad \rho_{zz} = -\frac{1}{4}\bar{v}_1\bar{v}_2, \quad (\text{A7})$$

all other terms of  $\rho_{\alpha\beta}$  being zero. For the degenerate case  $\rho_\infty$  is the same with the replacement  $\bar{v}_1, \bar{v}_2 \mapsto \bar{v}$ . (At the symmetric point  $\lambda_1 = \lambda_2$  there is an additional solution for  $\rho_\infty$  involving a dark state [25]; we do not consider here this special situation that needs fine tuning.)

- 
- [1] J. Wrachtrup, C. von Borczyskowski, J. Bernard, M. Orrit, and R. Brown, Optical detection of magnetic resonance in a single molecule, *Nature (London)* **363**, 244 (1993); Optically Detected Spin Coherence of Single Molecules, *Phys. Rev. Lett.* **71**, 3565 (1993).
- [2] J. Köehler, J. A. J. M. Disselhorst, M. C. J. M. Donckers, E. J. J. Groenen, J. Schmidt, and W. E. Moerner, Magnetic resonance of a single molecular spin, *Nature (London)* **363**, 242 (1993).
- [3] D. Rugar, R. Budakian, H. J. Mamin, and B. W. Chui, Single spin detection by magnetic resonance force microscope, *Nature (London)* **430**, 329 (2004).
- [4] J. M. Elzerman, P. Hanson, L. H. Willems van Beveren, B. Witkamp, L. M. K. Vandersypen, and L. P. Kouwenhoven, Single shot read-out of an individual electron spin in a quantum dot, *Nature (London)* **430**, 431 (2004).
- [5] M. Xiao, I. Martin, E. Yablonovitch, and H. W. Jiang, Electrical detection of the spin resonance of a single electron in a silicon-field effect transistor, *Nature (London)* **430**, 435 (2004).
- [6] Y. Manassen, E. Ter-Ovanesyan, D. Shachal, and S. Richter, Electron-spin resonance-scanning tunneling microscopy experiments on thermally oxidized Si(111), *Phys. Rev. B* **48**, 4887 (1993).
- [7] Y. Manassen, Real-time response and phase-sensitive detection to demonstrate the validity of ESR-STM results, *J. Magn. Reson.* **126**, 133 (1997).
- [8] Y. Manassen, I. Mukhopadhyay, and N. Ramesh Rao, Electron-spin-resonance STM on iron atoms in silicon, *Phys. Rev. B* **61**, 16223 (2000).
- [9] C. Durkan and M. E. Welland, Electronic spin detection in molecules using scanning-tunneling microscopy assisted electron-spin resonance, *Appl. Phys. Lett.* **80**, 458 (2002).
- [10] C. Durkan, Detection of single electronic spins by scanning tunneling microscopy, *Contemp. Phys.* **45**, 1 (2004).
- [11] T. Komeda and Y. Manassen, Distribution of frequencies of a single precessing spin detected by scanning tunneling microscope, *Appl. Phys. Lett.* **92**, 212506 (2008).
- [12] Y. Sainoo, H. Isshiki, S. M. F. Shahed, T. Takaoka, and T. Komeda, Atomically resolved Larmor frequency detection on Si(111)- $7 \times 7$  oxide surface, *Appl. Phys. Lett.* **95**, 082504 (2009).
- [13] A. V. Balatsky, M. Nishijima and Y. Manassen, Electron spin resonance scanning tunneling microscopy, *Adv. Phys.* **61**, 117 (2012).
- [14] Y. Manassen, M. Averbukh and M. Morgenstern, Analyzing multiple encounter as a possible origin of electron spin resonance signals in scanning tunneling microscopy on Si(111) featuring C and O defects, *Surf. Sci.* **623**, 47 (2014).
- [15] S. Müllegger, S. Tebi, A. K. Das, W. Schöffberger, F. Faschinger, and R. Koch, Radio Frequency Scanning Tunneling Spectroscopy for Single-Molecule Spin Resonance, *Phys. Rev. Lett.* **113**, 133001 (2014).
- [16] S. Baumann, W. Paul, T. Choi, C. P. Lutz, A. Ardavan, and A. J. Heinrich, Electron paramagnetic resonance of individual atoms on a surface, *Science* **350**, 417 (2015).
- [17] P. Willke *et al.*, Probing quantum coherence in single-atom electron spin resonance, *Sci. Adv.* **4**, eaaq1543 (2018).
- [18] T. S. Seifert, S. Kovarik, C. Nistor, L. Persichetti, S. Stepanow, P. Gambardella, Single-atom electron paramagnetic resonance in a scanning tunneling microscope driven by a radiofrequency antenna at 4K, *Phys. Rev. Research* **2**, 013032 (2020).
- [19] Y. Manassen, M. Averbukh, M. Jbara, B. Siebenhofer, A. Shnirman, B. Horovitz, Fingerprints of single nuclear spin energy levels using STM-ENDOR, *J. Magn. Reson.* **289**, 107 (2018).
- [20] A. Caso, B. Horovitz and L. Arrachea, Model for electron spin resonance in STM noise, *Phys. Rev. B* **89**, 075412 (2014).
- [21] A. Golub and B. Horovitz, Nanoscopic interferometer model for spin resonance in current noise, *Phys. Rev. B* **88**, 115423 (2013).
- [22] A. V. Balatsky, Y. Manassen, and R. Salem, Exchange-based noise spectroscopy of a single precessing spin with scanning tunnelling microscopy, *Philos. Mag.* **82**, 1291 (2002); ESR-STM of a single precessing spin: Detection of exchange-based spin noise, *Phys. Rev. B* **66**, 195416 (2002).
- [23] Y. Manassen and A. V. Balatsky,  $1/f$  Spin Noise and a Single Spin Detection with STM, *Israel J. Chem.* **44**, 401 (2004).
- [24] B. Horovitz and A. Golub, Double quantum dot scenario for spin resonance in current noise, *Phys. Rev. B* **99**, 241407(R) (2019).
- [25] B. Horovitz and C. Henkel, Spin entanglement via scanning tunneling microscope current, *Phys. Rev. B* **104**, L081405 (2021).
- [26] S. Buchholz, H. Fuchs, and J. P. Rabe, Surface structure of thin metallic films on mica as seen by scanning tunneling microscopy, scanning electron microscopy, and low energy electron diffraction, *J. Vac. Sci. Technol. B* **9**, 857 (1991).

- [27] J. L. Pitters, P. G. Piva, X. Tong, and R. A. Wolkow, Reversible Passivation of Silicon Dangling Bonds with the Stable Radical TEMPO, *Nano Lett.* **3**, 1431 (2003).
- [28] Z. Zhang, A. Berg, H. Levanon, R. W Fessenden and D. Meisel, On the interactions of free radicals with gold nanoparticles, *J. Am. Chem. Soc.* **125**, 7959 (2003).
- [29] H. Kobayashi, T. Ueda, K. Miyakubo, T. Eguchi, and A. Tani, ESR study of molecular dynamics and orientation of TEMPO included in organic 1-D nanochannel, *Phys. Chem. Chem. Phys.* **10**, 1263 (2008).
- [30] L. A. O'Dell and R. W. Schurko, Static solid-state  $^{14}\text{N}$  NMR and computational studies of nitrogen EFG tensors in some crystalline amino acids, *Phys. Chem. Chem. Phys.* **11**, 7069 (2009).
- [31] A. C. Hewson, *The Kondo Problem to Heavy Fermions* (Cambridge University Press, Cambridge, 1993).
- [32] J. E. Wertz and J. R. Bolton, in *Electron Spin Resonance, Elementary Theory and Practical Applications* (McGraw-Hill, New York, 1986), Chap. 10, Figs. 10–15b.